



Fermi National Accelerator Laboratory

FERMILAB-FN-626

Di-jet Mass Resolution at High Luminosity in the CMS Calorimeter

A. Beretvas, D. Green, J. Marraffino and W. Wu

*Fermi National Accelerator Laboratory
P.O. Box 500, Batavia, Illinois 60510*

October 1994

Disclaimer

This report was prepared as an account of work sponsored by an agency of the United States Government. Neither the United States Government nor any agency thereof, nor any of their employees, makes any warranty, express or implied, or assumes any legal liability or responsibility for the accuracy, completeness, or usefulness of any information, apparatus, product, or process disclosed, or represents that its use would not infringe privately owned rights. Reference herein to any specific commercial product, process, or service by trade name, trademark, manufacturer, or otherwise, does not necessarily constitute or imply its endorsement, recommendation, or favoring by the United States Government or any agency thereof. The views and opinions of authors expressed herein do not necessarily state or reflect those of the United States Government or any agency thereof.

Di-jet Mass Resolution at High Luminosity in the CMS Calorimeter

A. BERETVAS, D. GREEN, J. MARRAFFINO AND W. WU

Fermi National Accelerator Laboratory

P. O. Box 500, Batavia, IL 60510

ABSTRACT

Using reasonable values for all the relevant parameters, we have simulated the behaviour of the CMS calorimeter for the case of the LHC operating at high luminosity. In particular, we have investigated the problems associated with the relatively large number of minbias events expected to accompany each “interesting” event, its effect on the calorimeter resolution and some techniques to reduce that effect. We find that, while it is possible to moderate the loss of resolution, it is not possible to recover the full resolution. Moreover, the detailed strategies are dependent on the physics processes being studied.

Introduction

We have previously studied the high luminosity pileup problems for the SDC detector.¹⁻² The problem will be more serious for the LHC experiment. The SSC design luminosity was $10^{33}\text{cm}^{-2}\text{sec}^{-1}$, but in the LHC, the highest luminosity is expected to be 17 times larger. In addition, the bunch crossing time is increased from 18.2 nsec at the SSC to 30 nsec in LHC. Consequently, the mean number of overlapping minbias events per bunch crossing in the LHC could be $17 \times 30/18.2$ or 28 times larger than in the SSC. In SDC, we expected about 1.8 minbias events to overlap each “interesting” event ($100\text{mb} \times 10^{33}\text{cm}^{-2}\text{sec}^{-1} \times 18.2\text{nsec}$). In the CMS case, the number could be as high as 51, assuming the same total cross section. Therefore it is even more important to understand how the CMS calorimeter behaves at such high luminosities. In order to reduce the computing time in this simulation, we have estimated the number of overlap events using a Poisson distribution with a mean of 30. In our previous study for the SDC detector, we used 15 overlapping events in the high luminosity case.

The physics processes we are studying are low mass, low p_t di-jets and high p_t di-jets, as well as high mass di-jets from Drell-Yan Z' production. Low p_t means that the event generator was restricted to the p_t interval from 50 GeV/c to 60 GeV/c, and high p_t means that the generator was restricted to the p_t interval from 500 GeV/c to 600 GeV/c. For the high mass events, the generator was required to produce an object with a mass in the interval from 3 TeV to 4 TeV. The minbias events are QCD di-jets with p_t in the region 2 - 500 GeV/c. All events are generated by ISAJET version 6.36.

Mass Resolution vs the Cone Size

The reconstructed mass is formed by using di-jet momentum vectors whose magnitudes scale with the energy deposited within a cone. The direction of the vector is defined by that of the initial parton. We are also able to use a clustering method³ to determine the jet direction and reconstruct the mass. Since the results are very similar for the two methods, we have chosen not to use the clustering method (except as noted below in the section on Calorimeter Segmentation) in order to reduce the computing time in this study. Since high p_t jets are very strongly boosted, we take a single vector along the boost direction and simply compute the mass within the selected cone.

The best way to quantify the mass resolution is to use the ratio of the reconstructed mass to the generated mass so that the uncertainty due to the natural width of the Z' will be cancelled. The granularity of the CMS hadronic calorimeter (HAD) was taken to be 0.1×0.1 in η and ϕ , and 0.05×0.05 for the electromagnetic calorimeter (EM). The magnetic field is taken as 4 Tesla and the η coverage as $|\eta| \leq 1.5$. This η interval was chosen to allow direct comparison of the results obtained here with those of a previous study of the proposed SDC calorimeter⁴ which was limited to the barrel part of the calorimeter. We parametrize the hadronic and EM calorimeter resolution in the usual way by an expression of the form $dE/E = A/\sqrt{E} \oplus B$ where \oplus indicates that the two terms are added in quadrature. These two contributions are generally called the stochastic term and the constant term respectively. We have chosen $A = 0.6$ and $A = 0.03$ for the stochastic term for the HAD and EM calorimeter, and $B = 0.03$ and $B = 0.005$ for the constant term for the HAD and EM calorimeter. We also suppose the calorimeter is deep enough that there is no leakage. The cone radius, defined as $R = \sqrt{\Delta\eta^2 + \Delta\phi^2}$, varies from $R = 0.4$ to $R = 1.1$ except for a few cases where it was necessary to go slightly outside of this range to identify the best resolution.

The mass resolution vs the cone size for different physics processes, excluding

and including overlapping background events, is shown in Tables 1 through 6 for low mass low p_t , high p_t and high mass di-jets respectively. The various cases mentioned in the table headings are

- Case 1 corresponds to a perfect detector, no magnetic field and no contribution to the jet from the underlying event.
- Case 2 is the same as Case 1 but with the contribution to the jet from the underlying event included.
- Case 3 corresponds to the real detector, including resolution as described earlier, no cracks, no magnetic field but with the contribution to the jet from the underlying event included.
- Case 4 is the same as Case 3 but with the full 4 Tesla magnetic field.
- Case 5 is the same as Case 4 plus an additional tower threshold requirement of $E_T \geq 0.3$ GeV for the low p_t events and $E_T \geq 1.0$ GeV for the high p_t and high mass events.
- Case 6 is the same as Case 3 with the addition of $\bar{n} = 30$ overlapping minbias events.
- Case 7 is the same as Case 4 with the addition of $\bar{n} = 30$ overlapping minbias events.
- Case 8 is the same as Case 5 with the addition of $\bar{n} = 30$ overlapping minbias events.

Typical reconstructed mass plots for Case 5 with cone sizes ranging from 0.3 to 0.9 are shown in Figure 1 for high p_t jets. The full set of results is summarized in the tables. Tables 1, 2 and 3 show the results without any overlapping events, *i.e.*, Cases 1 through 5. There, we see that the underlying event is the dominant effect. For Case 1, where the underlying event is not considered, the mass resolution decreases monotonically with increasing cone size. This behaviour, shown in Figure 2, represents an intrinsic property of the physics process under consideration and, as such, is a natural limit on the mass resolution. For all other

cases, the resolution drops to a minimum and then increases again. Instrumental calorimeter energy resolution, magnetic field and threshold E_T cuts do affect the mass resolution but those effects are smaller than that due to the underlying event. This means that the mass resolution basically depends on the physics itself and pushing the detector performance for very high quality does not recover very much in mass resolution. Tables 4, 5 and 6 show, in adjacent columns, the comparison between excluding and including the contribution from minibias events. It is clear that including overlapping minibias events has a significantly degrading effect on the mass resolution for low p_t di-jets but a substantially smaller effect on the high p_t di-jet mass resolution, especially when a tower threshold cut is applied. These same effects are also summarized in Figures 3, 4 and 5 for low p_t , high p_t and high mass events respectively. Figure 6 shows the mass resolution obtained for all of the Cases enumerated above and for the three physics processes considered.

Clearly, a smaller cone size will exclude some signal energy, as is indicated by the mean value of the mass ratio being less than 1.0, and therefore worsen the mass resolution. On the other hand, too large a cone will pick up a significant contribution from overlap events, as indicated by the mean value of the mass ratio being greater than 1.0, and again worsen the mass resolution. We can also see that it is necessary to optimize the cone size for each physics process and luminosity to obtain the best mass resolution. The best cone size for a standard Z is $R \approx 0.6$, but somewhat larger for a heavy Z' as in our 3 TeV case. Since the pileup contribution for the Z' is small compared to the signal itself, only when the cone size is as large as 1.1, do we start to see the mass resolution worsen.

Minbias Effect

When we overlap the signal events with $\bar{n} = 30$ minbias events, we see that the mass resolution is badly degraded. Not surprisingly, the situation is worst for a cone size of 0.9 to 1.1, where the mean value of the mass ratio is as large as about 2 for high p_t events and about 3 for low p_t events, meaning that there is as much or more energy inside the cone from pileup as from signal.

As we can see from Tables 4, 5 and 6, it is still possible to find a best cone, but it has a rather smaller radius ($R \approx 0.3$) compared to the case without minbias ($R \approx 0.6$) for the low p_t di-jets. For high p_t di-jets, minbias has a much smaller effect, particularly after a tower threshold cut, and the no-minbias mass resolution is almost recovered. A typical LEGO plot of total energy deposit with minbias background is shown in Figure 7. One can see that there are small contributions from many towers as the “background” spreads over the LEGO plot.

Magnet Field Effect

In a previous study,⁵ we have noted that electron isolation from b decay is significantly improved by the magnetic field effect because some hadrons initially associated with the b decay can be swept away from the electron by the solenoidal field. In the case of the di-jet mass resolution, the benefit of the magnet field is not obvious. Some charged particles properly associated with the jet are swept out of the jet cone while other charged particles, not properly associated with the jet, are swept into the cone. Both of these processes represent a loss of physical information and lead us to expect a net worsening of the mass resolution. This expectation is verified as shown in Figure 8 where we have plotted the fractional mass resolution for low p_t and high p_t jets for our cases 3 and 4. These two cases differ only in that $B = 0$ for case 3 and $B = 4\text{ T}$ for case 4. It is clear that turning the magnet on never improves the resolution and does in fact worsen it for almost all values of the cone radius. We emphasize that neither of these cases

includes any overlapping minbias events and, therefore, even this comparison is somewhat idealized. The addition of overlapping minbias events will clearly worsen the resolution still further.

Tower Threshold Cut

In order to reduce the pileup, one can use a tower threshold cut, thereby preferentially reducing the contribution from minbias events. We note that a cone radius of 0.6 effectively integrates over ≈ 100 towers for the 0.1×0.1 segmentation of the CMS calorimeter. Thus a small per-tower contribution from these events can still add a substantial amount of energy.

In this study, we require $E_T \geq 0.3$ GeV per tower for low p_t jets, and 1.0 GeV per tower for high p_t and high mass jets. The optimized E_T threshold depends on both the physics process (low p_t or high p_t), and the luminosity, since it controls the amount of overlapping energy. Too high a threshold will reject signal, degrading the mass resolution, while too low a threshold will keep too much minbias contribution, again degrading the resolution. Moreover, the E_T threshold and the cone size are correlated. A lower threshold may require a slightly larger cone than the higher threshold in order to get optimal resolution, while a higher threshold may yield optimal mass resolution at slightly smaller cone radius. The optimal resolution is more or less the same with combinations of the optimal cone size and the threshold within reasonable variations.

We have tested this by using an $E_T \geq 2.0$ GeV threshold for high p_t jets and finding that the optimal cone size is smaller than with the $E_T \geq 1.0$ GeV threshold, but the resulting mass resolution is almost the same. The important point to this is that one can recover the mass resolution for high p_t jets by imposing threshold cuts, but still suffer for low p_t jet mass resolution because of the high luminosity. Figure 9 shows the effect of that cut for the same high p_t event as in Figure 7. As we have noted, the optimal cut will depend both on the physics process and the luminosity. Such a cut will degrade the mass resolution

for events without minbias overlap, since it will reject some signal. We notice that the mean value of the mass ratio is well below 1.0, even with the bigger cone size and especially for a standard Z. Nevertheless, this cut will benefit the cases where the minbias background is appreciable.

Calorimeter Segmentation

The kinematics of di-jets, ignoring fragmentation, implies that the mass resolution, dM , for a di-jet of mass M due to an angular error dq is given by

$$\frac{dM}{M} = \frac{p_t}{M} dq.$$

This lead us to expect that only highly boosted, light di-jets will have a significant contribution due to any angular error, and particularly that induced by calorimeter segmentation, compared to the energy error due to the calorimeter measurement. In our previous study for SDC (See Ref. 4), we found that the mass resolution depends very weakly on the granularity for low p_t jets and high mass jets, but the highly boosted standard Z shows a substantial effect due to segmentation.

We have made the same study for the low p_t and high p_t Z mass resolution as a function of the granularity and the results are shown in Table 7 and also in Figure 10. This study was made using release 6 of the CMS simulation program, CMSIM,⁶ which uses the clustering method. For the high p_t jets, the results are quite compatible with the results shown in Table 2 where the jet direction is defined as that of the initial parton. The low p_t jets are somewhat more sensitive to the details of the jet finding and reconstruction algorithm and, consequently, the resolution we obtain from CMSIM is slightly different from that shown in Table 1. Nevertheless, this difference does not alter the conclusion that the low p_t jet mass resolution is a very weak function of the calorimeter segmentation.

For $\delta\eta = \delta\phi < 0.1$, dM/M is weakly rising, but worsens dramatically when $\delta\eta = \delta\phi > 0.1$. We conclude that $\delta\eta = \delta\phi = 0.1$ is still acceptable for the hadronic calorimeter segmentation even for the high p_t jets.

REFERENCES

1. Di-jet Spectroscopy at High Luminosity, Dan Green, FERMILAB-Conf-90-151, July 1990.
2. Hadronic and Electromagnetic Transverse Calorimetric Segmentation, W. Wu, A. Beretvas, D. Green and J. Marraffino, FERMILAB-FN-589, April 1992.
3. SSCSIM: Development and Use by the Fermilab SDC Group, Weimin Wu, *et al.*, Proceeding MC 93, International Conference on Monte-Carlo Simulation in High Energy Physics and Nuclear Physics, World Scientific Publishing, Tallahassee, Florida, USA, 22-26 Feb. 1993.
4. Jet Energy Resolution of the SDC Detector, A. Para, *et al.*, FERMILAB-TM-1720, December 6, 1990.
5. Study of the Isolation of the Electron from W and B Decay, Weimin Wu, Argonne/FNAL, SSC-SDC-F-83, June 30, 1991.
6. CMSIM-CMANA - CMS Simulation Facilities, C. Charlot, *et al.*, CMS TN/93-63, July 29, 1994.

Table 1. Fractional Reconstructed Mass and Mass Resolution for Low p_t Di-jets
Minbias Overlap Events Excluded

Radius	Case 1	Case 2	Case 3	Case 4	Case 5
0.4	0.79	0.84	0.80	0.82	0.74
0.5	0.83	0.89	0.84	0.86	0.77
0.6	0.87	0.92	0.88	0.89	0.80
0.7	0.88	0.96	0.91	0.92	0.82
0.8	0.90	1.00	0.94	0.96	0.83
0.9	0.92	1.03	0.97	0.99	0.86
1.0	0.92	1.07	1.01	1.03	–
1.1	0.93	1.12	1.04	1.08	–

Table 1a. Fractional Reconstructed Mass versus Cone Size.

Radius	Case 1	Case 2	Case 3	Case 4	Case 5
0.4	10.9	10.3	12.2	13.2	12.9
0.5	7.0	10.1	11.9	12.8	12.6
0.6	5.5	10.9	13.1	12.8	13.1
0.7	4.9	11.2	13.7	13.6	13.1
0.8	4.4	12.0	13.7	13.6	13.3
0.9	3.7	13.0	14.4	14.3	13.8
1.0	3.6	14.3	16.0	14.8	–
1.1	3.5	16.0	16.9	16.3	–

Table 1b. Fractional Reconstructed Mass Resolution in percent versus Cone Size.

Table 2. Fractional Reconstructed Mass and Mass Resolution for High p_t Di-jets
Minbias Overlap Events Excluded

Radius	Case 1	Case 2	Case 3	Case 4	Case 5
0.4	0.88	0.91	0.80	0.85	0.80
0.5	0.91	0.93	0.93	0.92	0.85
0.6	0.92	0.95	0.95	0.94	0.85
0.7	0.93	0.98	0.97	0.96	0.86
0.8	0.93	1.00	0.99	0.99	0.86
0.9	0.93	1.03	1.02	1.02	0.86
1.0	0.93	1.07	1.05	1.04	0.87
1.1	0.94	1.12	1.09	1.08	0.87

Table 2a. Fractional Reconstructed Mass versus Cone Size.

Radius	Case 1	Case 2	Case 3	Case 4	Case 5
0.4	9.3	7.7	9.9	15.8	15.6
0.5	7.4	7.0	9.5	10.8	11.8
0.6	6.3	7.9	8.9	10.1	10.5
0.7	5.9	8.2	8.6	10.1	10.5
0.8	5.6	9.5	9.1	10.3	11.4
0.9	5.5	11.2	10.4	12.0	11.7
1.0	5.4	14.1	12.5	12.6	11.8
1.1	5.4	16.1	15.0	15.0	12.5

Table 2b. Fractional Reconstructed Mass Resolution in percent versus Cone Size.

Table 3. Fractional Reconstructed Mass and Mass Resolution for High Mass Di-jets
Minbias Overlap Events Excluded

Radius	Case 1	Case 2	Case 3	Case 4	Case 5
0.4	0.97	–	0.96	–	0.96
0.5	0.97	0.97	0.97	0.98	0.97
0.6	0.99	0.98	0.98	1.00	0.98
0.7	1.00	1.00	0.99	1.00	0.98
0.8	1.00	1.00	1.00	1.01	0.99
0.9	1.01	1.01	1.01	1.02	0.99
1.0	1.01	1.02	1.01	1.02	1.00
1.1	1.01	1.02	1.02	1.03	1.00

Table 3a. Fractional Reconstructed Mass versus Cone Size.

Radius	Case 1	Case 2	Case 3	Case 4	Case 5
0.4	6.7	–	7.3	–	6.4
0.5	6.6	6.6	7.1	6.4	5.9
0.6	5.4	5.8	6.4	5.6	5.6
0.7	4.8	5.2	6.0	5.2	5.6
0.8	3.9	5.1	6.0	4.9	5.5
0.9	3.6	4.9	5.7	4.9	4.7
1.0	3.3	4.9	5.7	4.9	4.8
1.1	2.9	5.2	5.8	5.1	5.3

Table 3b. Fractional Reconstructed Mass Resolution in percent versus Cone Size.

Table 4. Fractional Reconstructed Mass and Mass Resolution for Low p_t Di-jets
Minbias Overlap Events Included

Radius	Case 3	Case 6	Case 4	Case 7	Case 5	Case 8
0.2	–	0.70	0.62	0.52	0.57	0.45
0.3	0.73	0.94	0.75	0.77	0.69	0.67
0.4	0.80	1.13	0.82	0.92	0.74	0.80
0.5	0.84	1.34	0.86	1.07	0.77	0.92
0.6	0.88	1.59	0.89	1.25	0.80	1.02
0.7	0.91	1.85	0.92	1.42	0.82	1.15
0.8	0.94	2.19	0.96	1.63	0.83	1.29
0.9	0.97	2.62	0.99	1.89	0.86	1.46
1.0	1.01	3.03	1.03	2.21	–	–

Table 4a. Fractional Reconstructed Mass versus Cone Size.

Radius	Case 3	Case 6	Case 4	Case 7	Case 5	Case 8
0.2	–	17.0	18.3	24.8	18.3	24.5
0.3	14.2	14.5	15.4	18.1	14.7	18.6
0.4	12.2	18.3	13.2	17.1	12.9	16.7
0.5	11.9	20.3	12.8	19.6	12.6	18.0
0.6	13.1	26.5	12.8	21.3	13.1	19.2
0.7	13.7	29.8	13.6	24.7	13.1	20.2
0.8	13.7	36.2	13.6	28.9	13.3	23.3
0.9	14.4	50.0	14.3	35.2	13.8	25.4
1.0	16.0	57.9	14.8	43.9	–	–

Table 4b. Fractional Reconstructed Mass Resolution in percent versus Cone Size.

Table 5. Fractional Reconstructed Mass and Mass Resolution for High p_t Di-jets
Minbias Overlap Events Included

Radius	Case 3	Case 6	Case 4	Case 7	Case 5	Case 8
0.4	0.90	0.93	0.85	0.91	0.80	0.83
0.5	0.93	1.04	0.92	1.01	0.85	0.88
0.6	0.95	1.14	0.94	1.09	0.85	0.80
0.7	0.97	1.29	0.96	1.19	0.86	0.91
0.8	0.99	1.49	0.99	1.33	0.86	0.94
0.9	1.02	1.72	1.02	1.51	0.86	0.98
1.0	1.05	2.02	1.04	1.72	0.87	1.01
1.1	1.09	2.38	1.08	1.95	0.87	1.08

Table 5a. Fractional Reconstructed Mass versus Cone Size.

Radius	Case 3	Case 6	Case 4	Case 7	Case 5	Case 8
0.4	9.9	12.6	15.8	12.2	15.6	12.2
0.5	9.5	10.2	10.8	10.4	11.8	10.1
0.6	8.9	12.3	10.1	11.1	10.5	10.5
0.7	8.6	13.9	10.1	12.6	10.5	11.9
0.8	9.1	19.2	10.3	16.8	11.4	12.4
0.9	10.4	27.2	12.0	20.2	11.7	14.5
1.0	12.5	30.6	12.6	26.6	11.8	16.2
1.1	15.0	35.7	15.0	34.3	12.5	18.8

Table 5b. Fractional Reconstructed Mass Resolution in percent versus Cone Size.

Table 6. Fractional Reconstructed Mass and Mass Resolution for High Mass Di-jets
Minbias Overlap Events Included

Radius	Case 3	Case 6	Case 4	Case 7	Case 5	Case 8
0.4	0.96	0.98	–	0.98	0.96	0.96
0.5	0.97	0.99	0.98	0.99	0.97	0.97
0.6	0.98	1.02	1.00	1.00	0.98	0.98
0.7	0.99	1.04	1.00	1.02	0.98	0.98
0.8	1.00	1.05	1.01	1.03	0.99	0.99
0.9	1.01	1.06	1.02	1.04	0.99	0.99
1.0	1.01	1.07	1.02	1.05	1.00	0.99
1.1	1.02	1.09	1.03	1.06	1.00	1.00

Table 6a. Fractional Reconstructed Mass versus Cone Size.

Radius	Case 3	Case 6	Case 4	Case 7	Case 5	Case 8
0.4	7.3	6.6	–	6.4	6.4	6.6
0.5	7.1	6.6	6.4	6.3	5.9	6.5
0.6	6.4	5.6	5.6	6.0	5.6	6.1
0.7	6.0	4.2	5.2	5.9	5.6	5.8
0.8	6.0	5.2	4.9	5.8	5.5	5.6
0.9	5.7	5.8	4.9	5.8	4.7	5.8
1.0	5.7	6.5	4.9	5.9	4.8	5.9
1.1	5.8	6.9	5.1	6.2	5.3	6.0

Table 6b. Fractional Reconstructed Mass Resolution in percent versus Cone Size.

Table 7. Fractional Reconstructed Mass Resolution for Boosted Jets

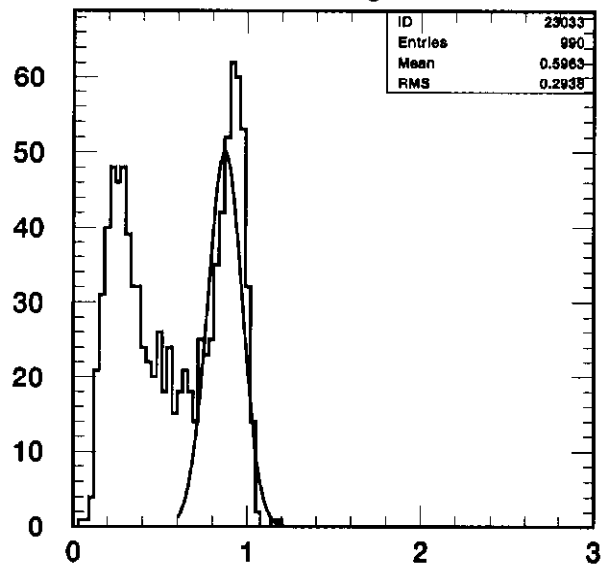
Granularity $\delta\eta = \delta\phi$	Granularity $\pi/(n \times m)$	dM/M at low p_t in percent	dM/M at high p_t in percent
0.037	12×7	15.4	6.4
0.048	11×6	15.6	6.8
0.063	10×5	15.9	7.0
0.087	9×4	16.2	7.6
0.131	8×3	16.5	10.1
0.157	4×5	16.6	13.7
0.196	8×2	16.7	18.0
0.224	7×2	17.8	25.2

FIGURE CAPTIONS

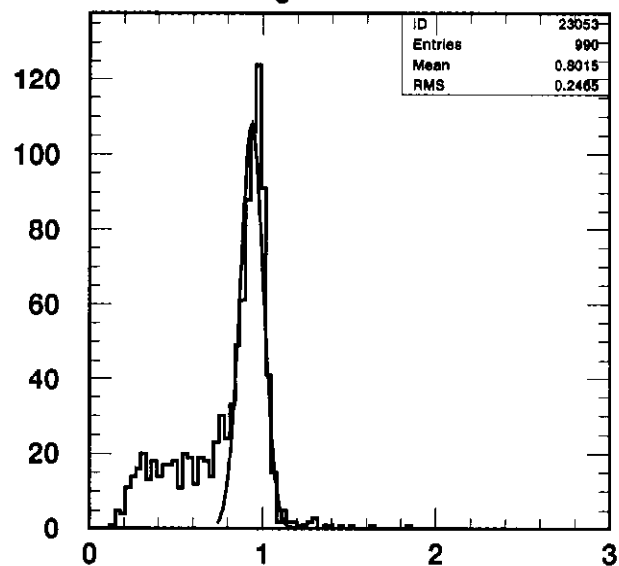
1. Ratio of reconstructed Z mass to generated Z mass in high p_t events for Case 5 with the jet cone radius varying from 0.3 to 0.9. The curve is the result of a gaussian fit over the restricted interval shown.
2. Reconstructed mass resolution for Case 1 (as described in the text) for low p_t , high p_t and high mass events.
3. Reconstructed mass resolution for low p_t events. The results for minbias overlap excluded, minbias overlap included and minbias overlap included with an E_T threshold are all shown.
4. Reconstructed mass resolution for high p_t events. The results for minbias overlap excluded, minbias overlap included and minbias overlap included with an E_T threshold are all shown.
5. Reconstructed mass resolution for high mass events. The results for minbias overlap excluded, minbias overlap included and minbias overlap included with an E_T threshold are all shown.
6. Reconstructed mass resolution for all 8 cases defined in the text and for each of the three physics processes considered. For comparison purposes, all three graphs are plotted on the same scale.
7. LEGO plot for a typical high p_t event with $\bar{n} = 30$ overlaid minbias events and no threshold cut. The energy deposition has been truncated at 50 GeV to make the towers with low energy deposition clearer.
8. Fractional mass resolution for low p_t and high p_t events as a function of cone radius comparing Case 3 (no magnetic field) and Case 4 (full 4 Tesla magnetic field).
9. LEGO plot for the same high p_t event as in Figure 7 but with a threshold E_T cut of 1.0 GeV. Again, the energy deposition has been truncated at 50 GeV to make the towers with low energy deposition clearer.

10. Fractional mass resolution for low p_t and high p_t standard Z as a function of calorimeter segmentation.

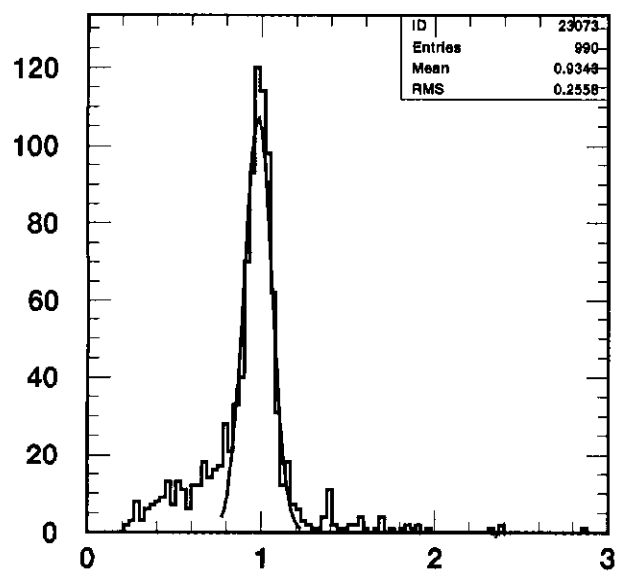
Figure 1. Mass ratio as a Function of R High Pt



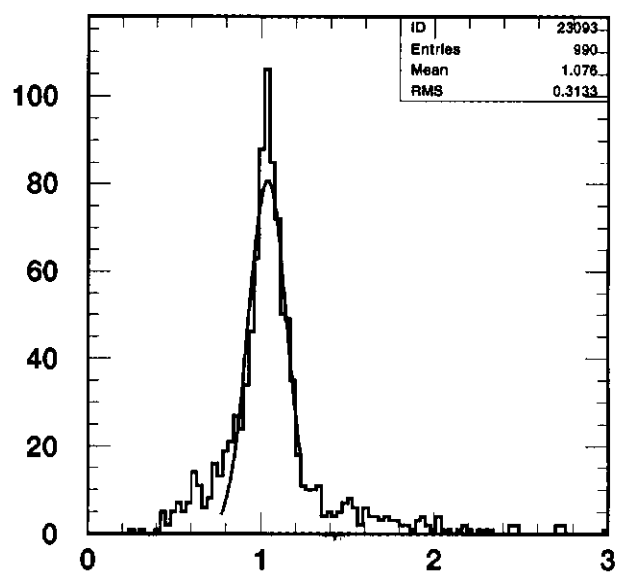
Mass Ratio for R = 0.3



Mass ratio for R = 0.5



Mass Ratio for R = 0.7



Mass Ratio for R = 0.9

Figure 2. Fractional Mass Resolution in percent for Case 1

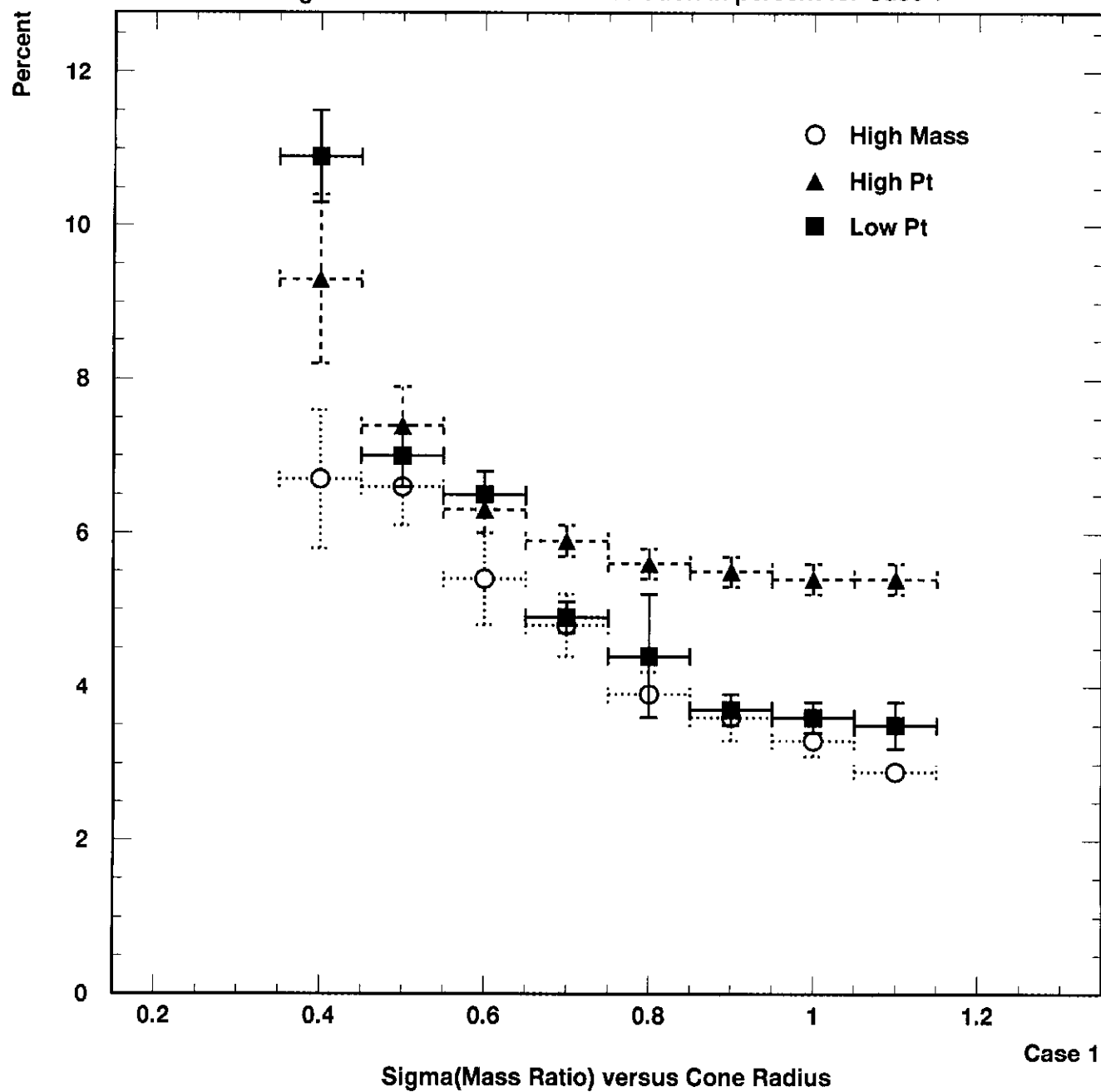


Figure 3. Fractional Mass Resolution in percent Low Pt

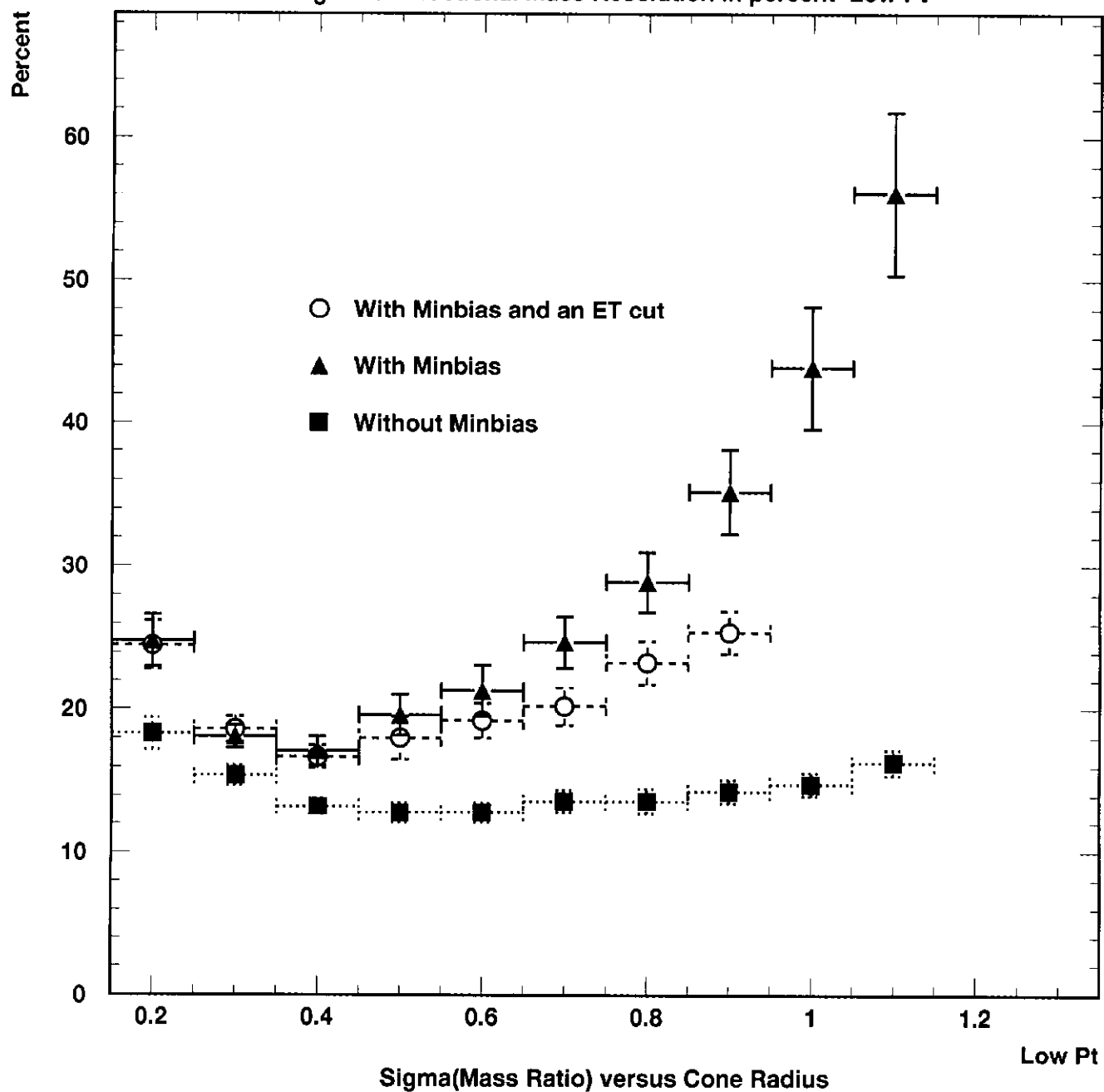


Figure 4. Fractional Mass Resolution in percent High Pt

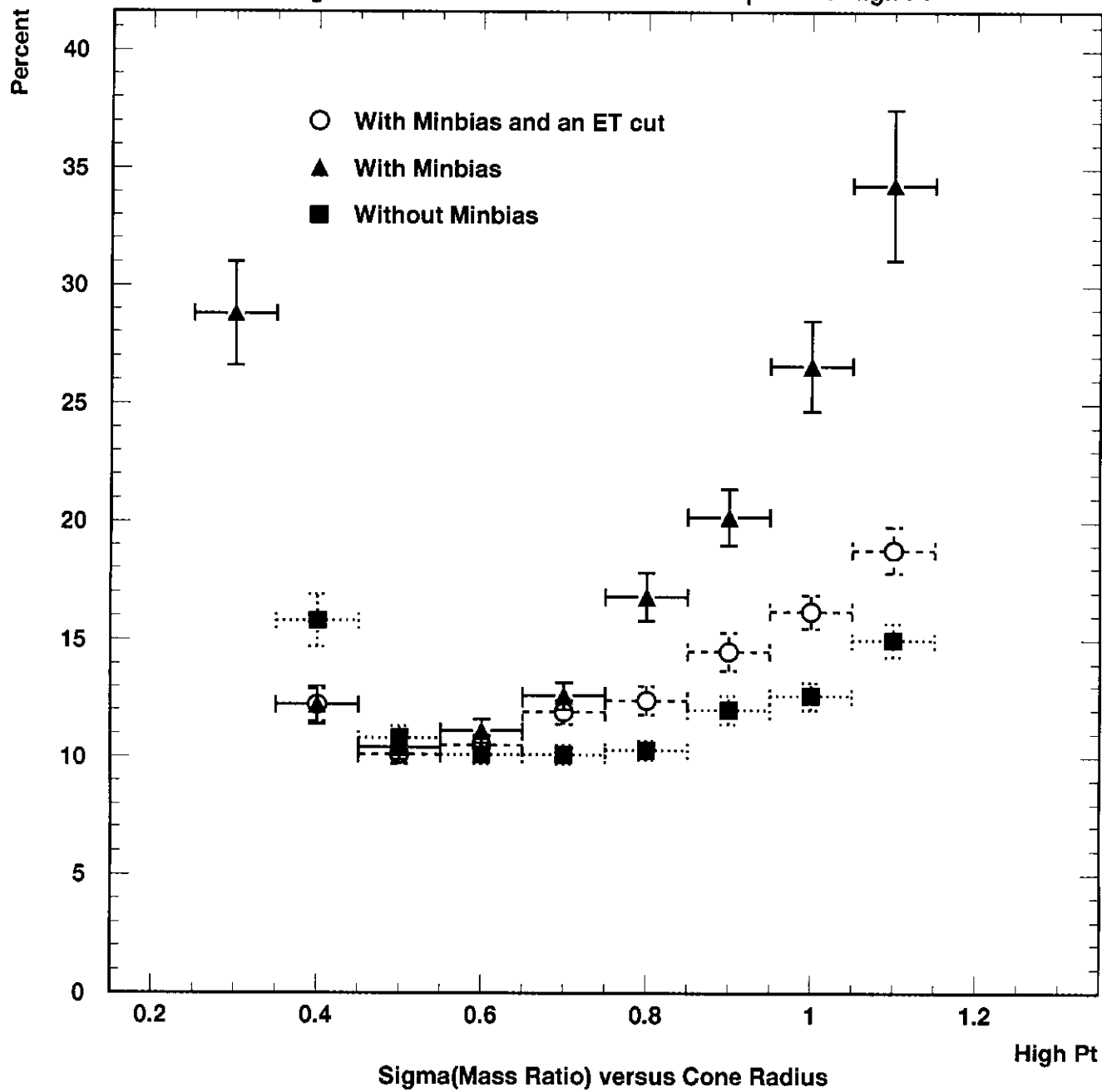


Figure 5. Fractional Mass Resolution in percent High Mass

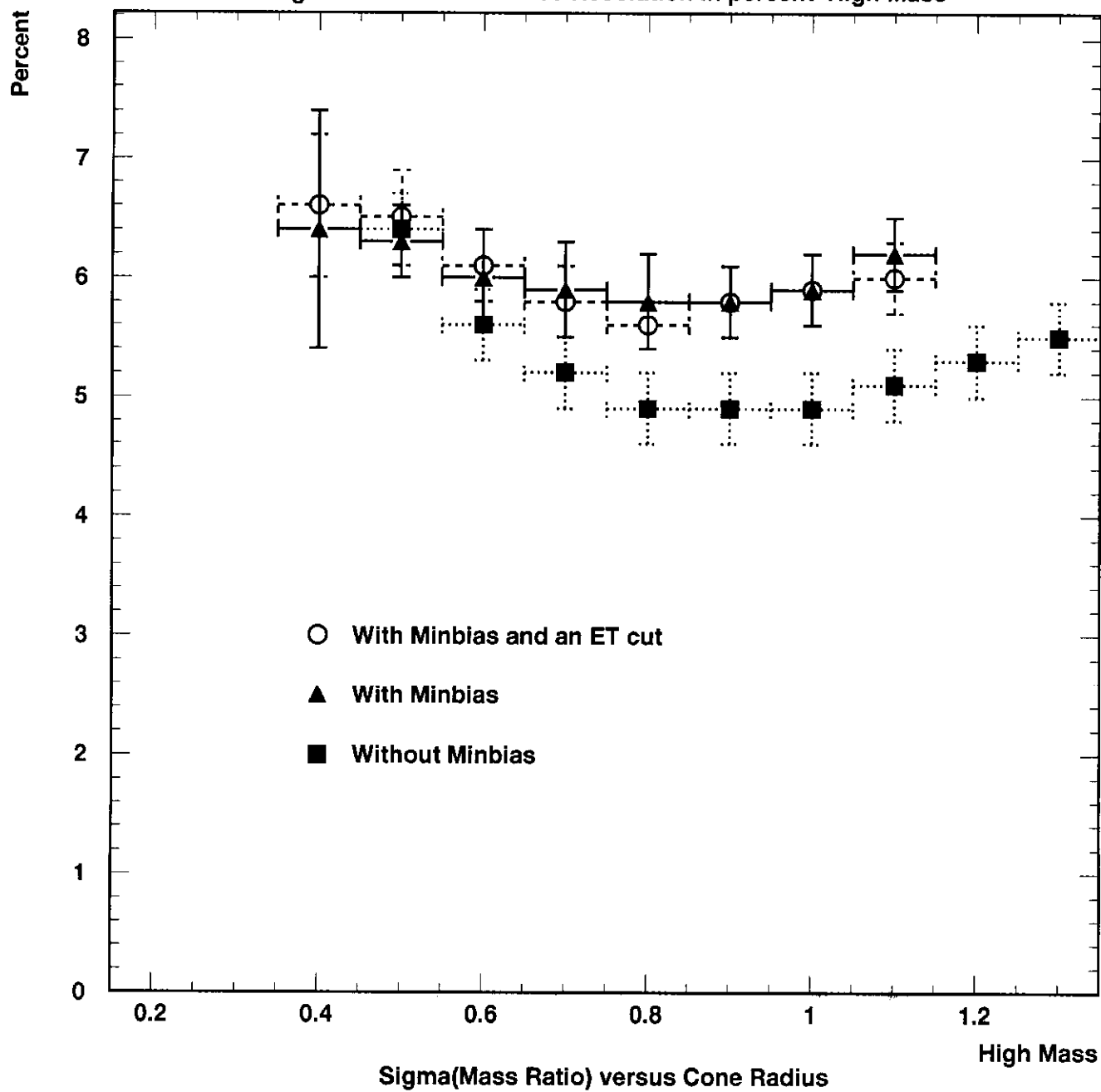


Figure 6. Fractional Mass Resolution in percent by Case

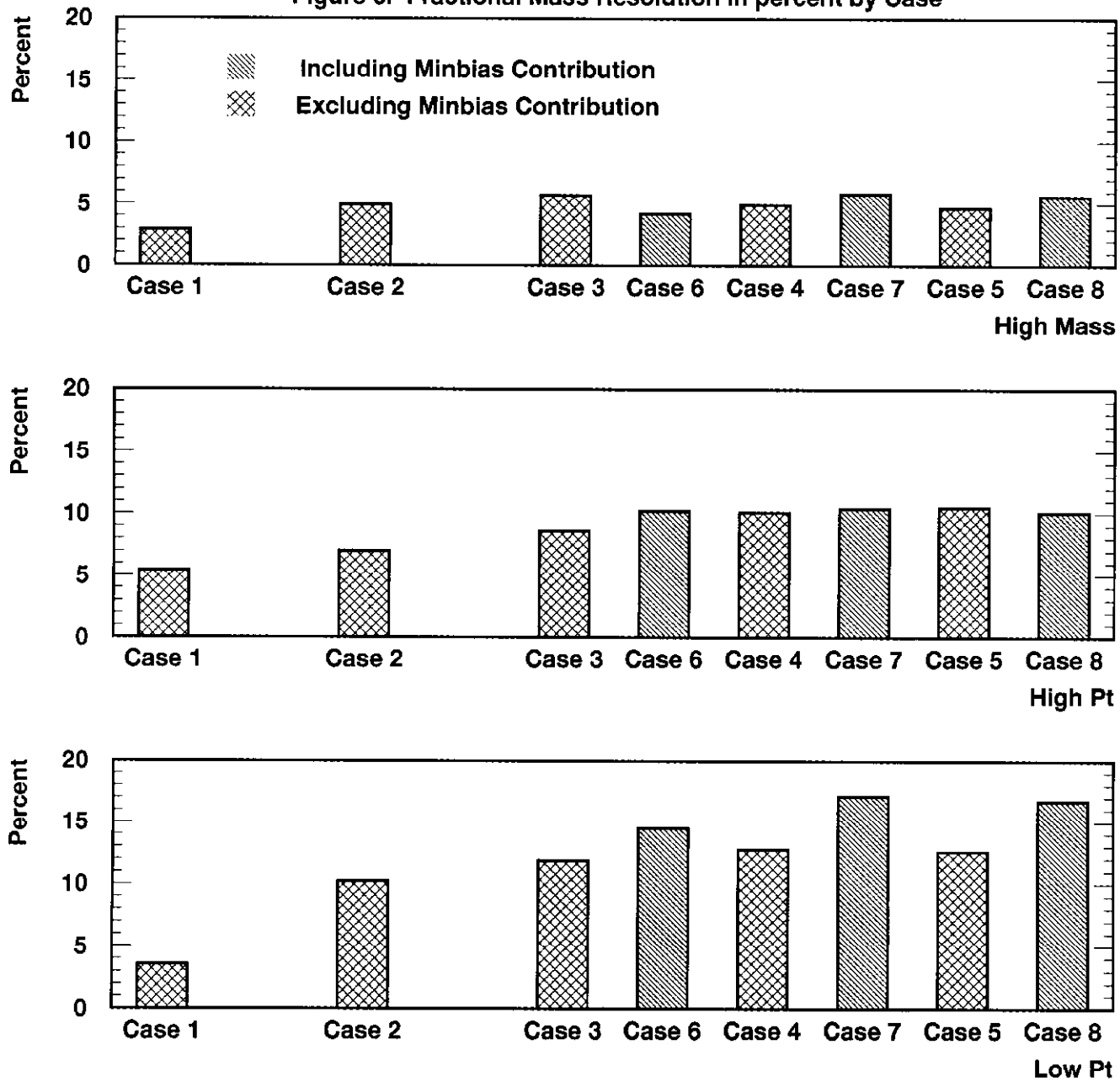


Figure 7. Total Energy Deposit in the Calorimeter

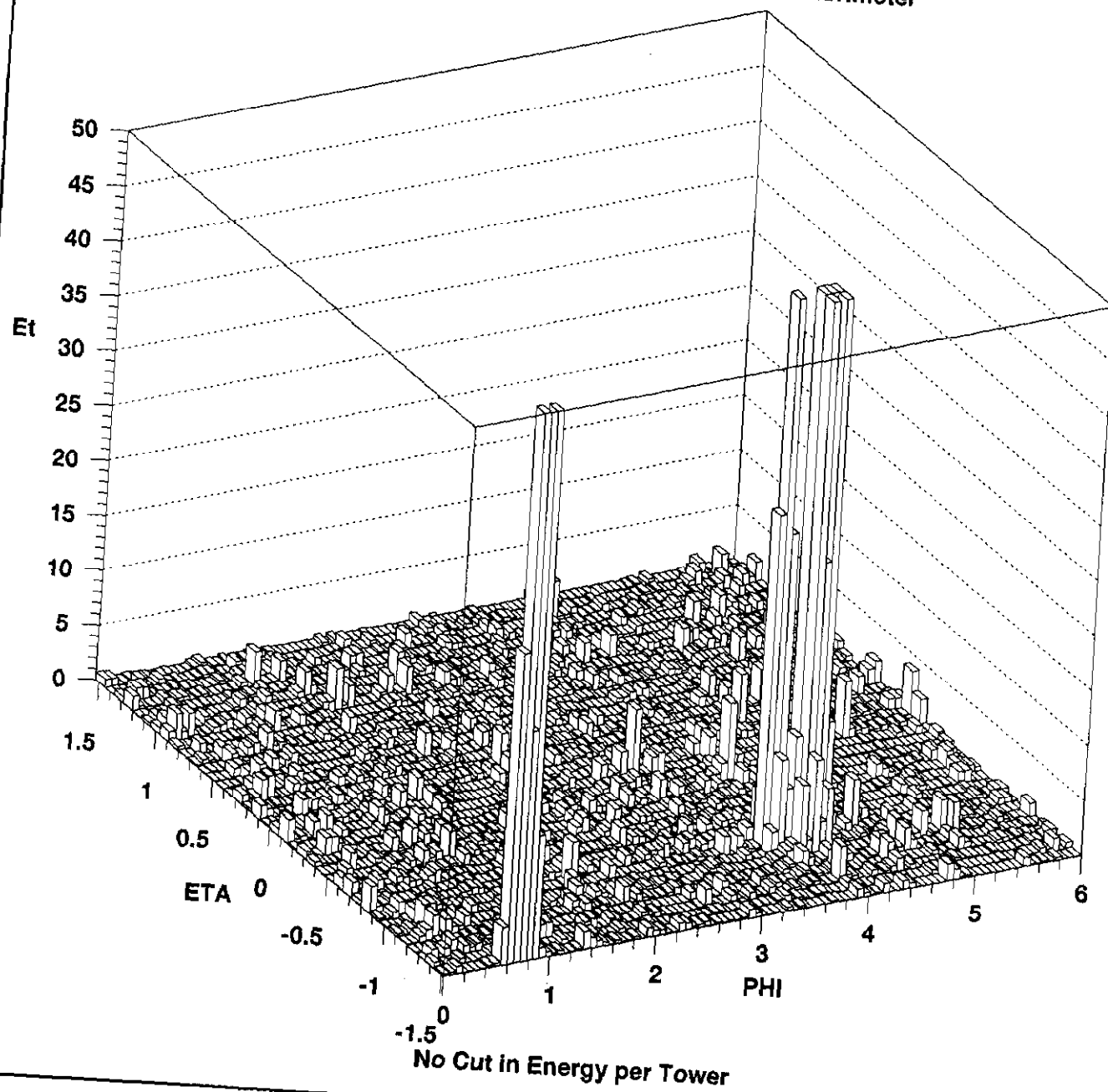


Figure 8. Fractional Mass Resolution in percent

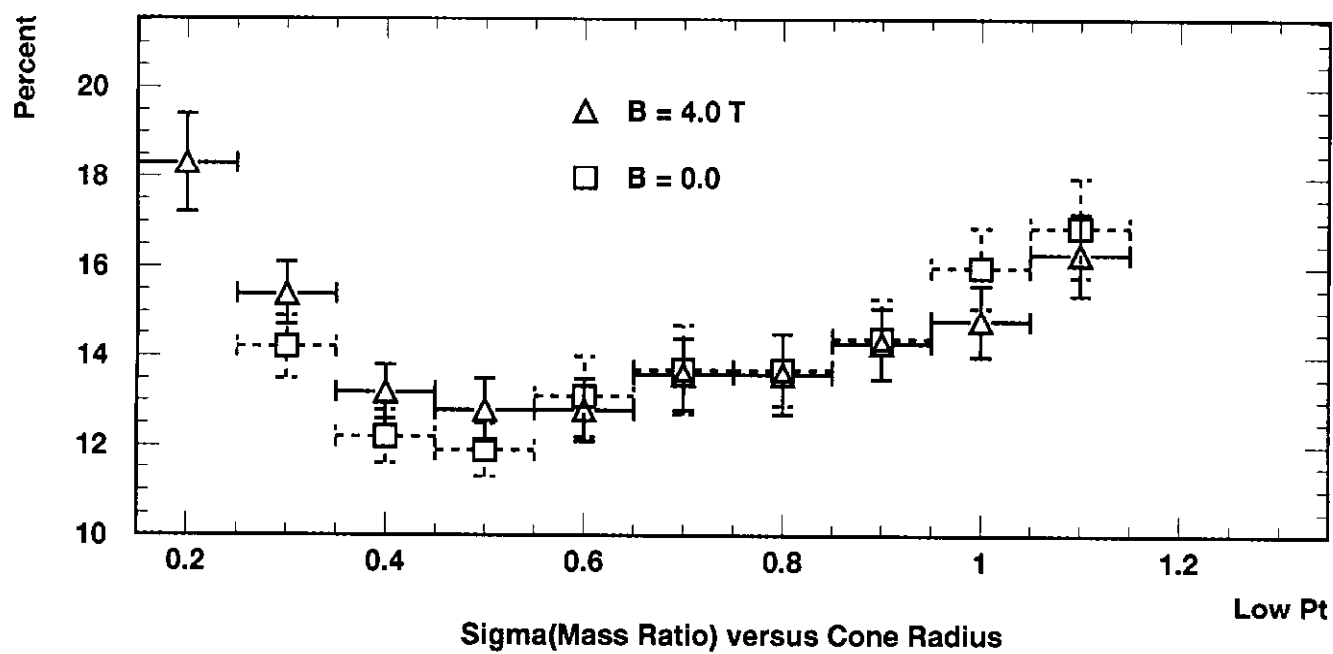
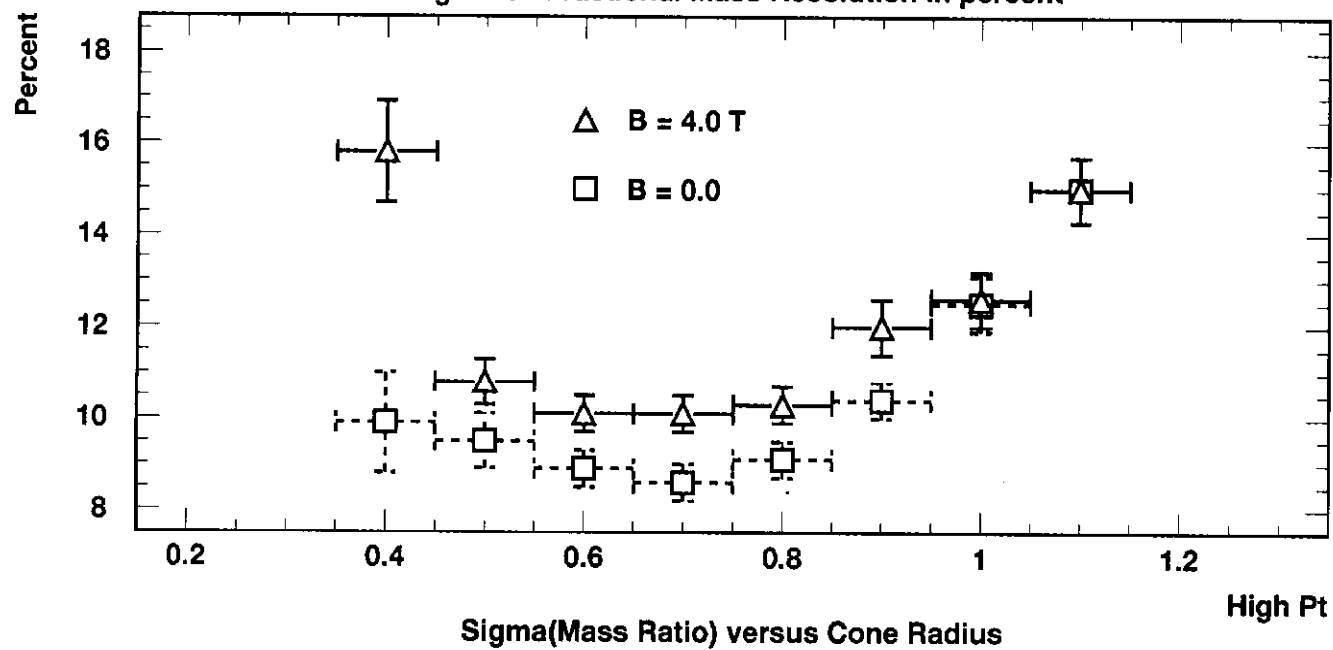


Figure 9. Total Energy Deposit in the Calorimeter

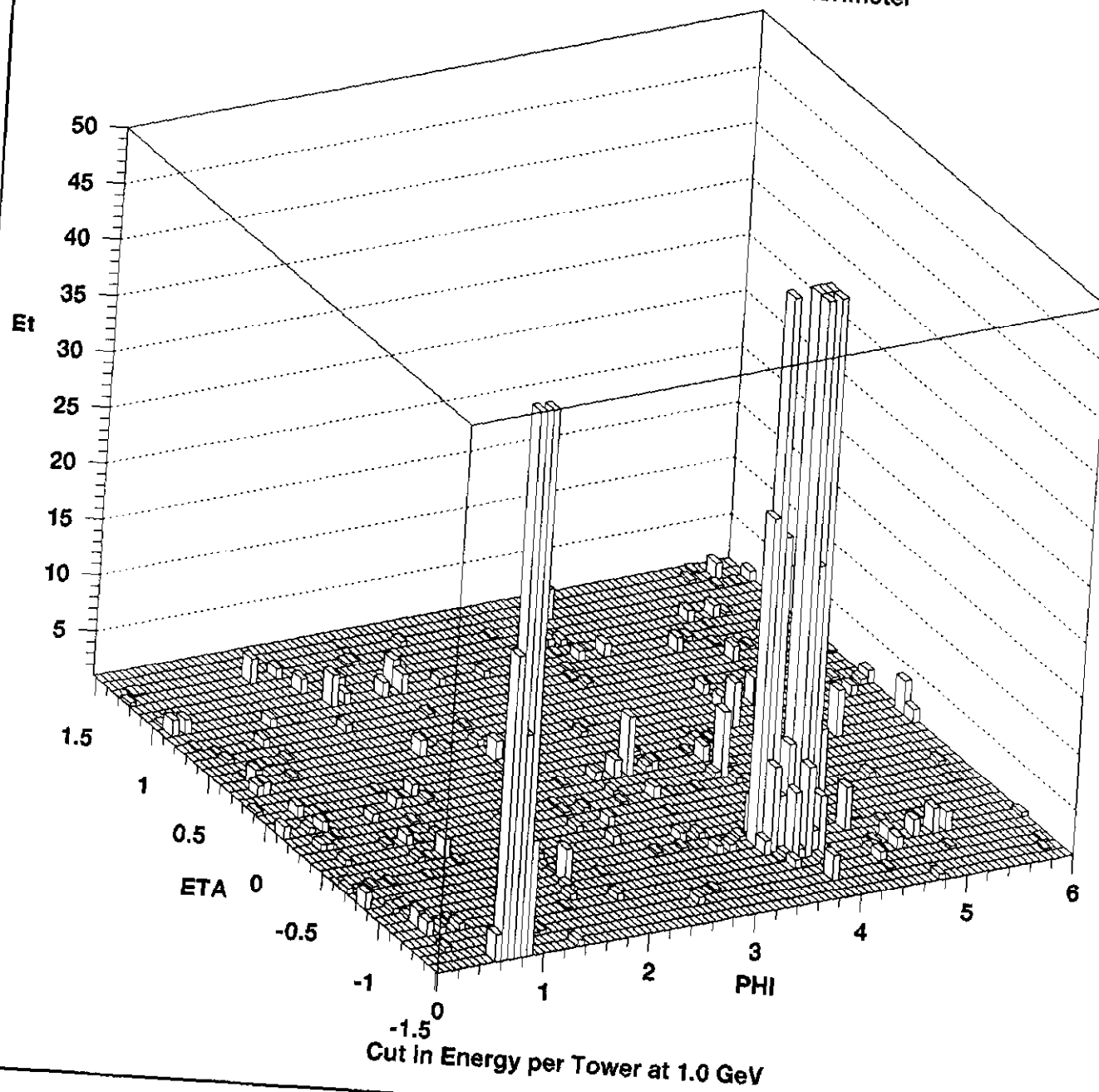


Figure 10. Fractional Mass Resolution vs Segmentation

